Speed-Dependent Anisotropy Parameters in the UV Photodissociation of Ozone

Ruth J. Wilson, Julie A. Mueller, and Paul L. Houston*

Department of Chemistry, Cornell University, Ithaca, New York 14853

Received: April 2, 1997; In Final Form: July 2, 1997[⊗]

Resonance-enhanced multiphoton ionization coupled with time-of-flight product imaging has been used to study the $O_2(^3\Sigma_g^-) + O(^3P_j)$ product channel in the UV photodissociation of ozone at photolysis wavelengths of 226, 230, 240, and 266 nm. For dissociation at 226 and 230 nm the $O(^3P_2)$ fragment is produced with a strongly bimodal velocity distribution, in keeping with the previous findings of Miller et al., Syage, and Stranges et al. at photolysis wavelengths of 226 and 193 nm. At the longer dissociation wavelengths of 240 and 266 nm, the bimodal velocity distribution becomes less evident in the $O(^3P_2)$ product. Anisotropy parameters have been determined as a function of the $O(^3P_2)$ fragment speed. A very similar and clear speed dependence is evident at all photolysis wavelengths considered, with the anisotropy parameters rising steadily as the oxygen atom speed increases. The UV dissociation dynamics of ozone to the channel producing triplet products are discussed in light of this analysis.

Introduction

The UV photodissociation of ozone via the intense Hartley absorption band (220−310 nm) proceeds predominantly along two spin-allowed product channels:

$$O_3 + h\nu \rightarrow O_2(a^1\Delta_g) + O(^1D) \qquad \sim 90\%$$

$$O_3 + h\nu \rightarrow O_2(X^3\Sigma_g^-) + O(^3P_j) \qquad \sim 10\% \qquad (1)$$

Here the major channel leading to singlet products correlates to the excited B^1B_2 surface populated directly by the $B^1B_2 \leftarrow \tilde{X}^1A_1$ electronic transition responsible for the Hartley absorption band.[1] The origin of the minor channel is more complex and is the result of a predissociative curve crossing between the excited-state surface and a repulsive $\tilde{R}$ state which leads to the triplet products.[1]

Considerable experimental effort has gone into determining the branching ratios of the two channels at a number of photolysis wavelengths within the Hartley band.[2−8] These studies are in general agreement and show the product yields to be independent of the dissociation energy between 220 and 305 nm. Observed yields were 0.85−0.90 and 0.15−0.1 for the $O(^1D)$ and $O(^3P_j)$ fragments, respectively.

Recently, the triplet channel has received additional attention because experimental studies have shown that, for photolysis at 226 and 193 nm, the $O(^3P_j)$ fragment is produced with a bimodal velocity distribution.[9−13] As a consequence of the laws of conservation of energy and momentum, the internal energy of the sibling $O_2(^3\Sigma_g^-)$ photofragment formed in coincidence must also exhibit a bimodal distribution. The original $O(^3P_j)$ product imaging experiments by Miller et al.[9] that uncovered the unexpected bimodal velocity distribution of the $O(^3P_j)$ were unable to ascertain whether the internal energy of the $O_2(^3\Sigma_g^-)$ fragment was electronic or vibrational. However, pump−probe experiments performed by the Wodtke group[9] demonstrated that highly vibrationally excited $O_2(^3\Sigma_g^-)$ is produced in the dissociation of ozone with a distribution matching the one predicted from the imaging experiments. Therefore, for photolysis at 226 nm Miller et al. concluded that the $O_2(^3\Sigma_g^-)$ vibrational distribution is bimodal with peaks at both $v = 14$ and $v = 27$.

The discovery that $O_2(^3\Sigma_g^-, v \geq 26)$ is formed in the UV photodissociation of ozone has had important consequences for modeling the stratospheric ozone budget,[9,14,15] since an additional odd oxygen production channel is thought to open,[16]

$$O_2(X^3\Sigma_g^-, v \geq 26) + O_2 \rightarrow O_3 + O \qquad (2)$$

Incorporating this additional ozone into atmospheric models of stratospheric ozone concentrations has made inroads into the long-standing and perplexing "ozone deficit" problem. This deficit refers to the mismatch between measured stratospheric ozone concentrations and modeled ones, with the modeled values falling consistently short of the measured quantities.[17,18] There is some debate over the magnitude of the discrepancy,[19−22] but it does appear that minor ozone production sources may have been overlooked in previous models. To build a more accurate picture of the ozone budget and to investigate the impact the additional channel will have on it, the wavelength dependence of $O_2(^3\Sigma_g^-, v \geq 26)$ is required. The measurement of this dependence is underway and will be presented in future work.

The investigation presented here is an attempt to unravel the underlying dynamics that lead to the striking bimodal velocity distribution observed in the $O(^3P_2)$ image for dissociation at 226 nm. Time-of-flight product imaging[23] permits simultaneous sampling of the complete speed and angular distributions of the state-selected $O(^3P_j)$ fragment. Examination of the $O(^3P_2)$ angular distributions allows us to determine laboratory frame anisotropy parameters (β) as a function of photolysis wavelength, providing information on the parent molecule geometry immediately prior to dissociation. Furthermore, the angular distributions can be easily analyzed as a function of $O(^3P_2)$ fragment speed. It is hoped that the resulting anisotropy parameters obtained as functions of both photolysis wavelength and $O(^3P_2)$ fragment speed will give some insight into the dynamics of the photolysis mechanism or mechanisms active in the dissociation channel of ozone that leads to triplet products.

Experimental Section

The product imaging experimental details have been described more fully elsewhere.[9,24] A molecular beam of ozone was formed by flowing He over ozone maintained on silica gel at a

[⊗] Abstract published in *Advance ACS Abstracts,* September 15, 1997.

S1089-5639(97)01158-4 CCC: $14.00

temperature of −34 °C. The resulting gas mix (∼10% ozone) was expanded through a pulsed 250 μm diameter nozzle and collimated by a 500 μm diameter skimmer mounted a few millimeters from the nozzle orifice. Further downstream, the molecular beam was crossed at right angles by two counter-propagating laser beams, one serving to dissociate the ozone and the other to probe the resulting $O(^3P_2)$ fragments using the $O(3p\ ^3P_2 \leftarrow\leftarrow 2p\ ^3P_2)$ 2 + 1 REMPI scheme near 226 nm. Due to the large Doppler width of the $O(^3P_2)$ fragments, it was necessary to scan the probe laser over the resonance to ensure that the images include all product $O(^3P_2)$ atom velocities.

Depending on photolysis wavelength, two separate methods were employed to generate the dissociating light. Radiation at 230 and 240 nm was produced by frequency doubling the output of an optical parametric oscillator (Spectra-Physics MOPO-730) pumped by an injection-seeded Nd:YAG (Spectra Physics GCR-230). Light at 266 nm was produced by the fourth harmonic of an injection seeded Nd:YAG (Spectra-Physics DCR-4). Typical laser powers were 3 and 5 mJ/pulse for the 230/240 and 266 nm radiation, respectively, with a pulse length of 8−10 ns.

The tunable light needed to probe the $O(^3P_2)$ fragments at 226 nm was generated by frequency doubling the output of an injection-seeded, Nd:YAG-pumped dye laser and then summing the doubled light with the Nd:YAG laser fundamental; typical powers achieved were 1.5 mJ/pulse with a pulse length of 8−10 ns. For studies of photodissociation at 226 nm, this laser served as both the photolysis and the probe laser. Photolysis and probe beams were directed into the vacuum chamber and focused onto the interaction zone by 25 and 7.5 cm focal length plano-convex lenses, respectively.

For data collected at dissociation wavelengths of 226, 230, and 240 nm an electrostatic lens was employed that served both to extract the ionized $O(^3P_2)$ fragments from the interaction zone and to deblur the image. This technique of velocity mapping[25] greatly increases the resolution of the images. For data collected at a dissociation wavelength of 266 nm no electrostatic lens was used. Instead, the ionized fragments were extracted from the interaction zone using more conventional repeller plates. The ionized fragments were accelerated into a Wiley-McLaren time-of-flight mass spectrometer mounted with its flight direction along the axis of the molecular beam. The ions were imaged by a position sensitive detector, consisting of a double microchannel plate assembly coupled to a fast phosphor screen. The image on the phosphor screen was recorded by a 640 × 480 pixel charge coupled device (CCD) camera electronically shuttered to collect signal corresponding to the mass of the oxygen atoms. Images were accumulated in real time into a 32-bit buffer, and a background signal was also taken for the same number of laser shots with the molecular beam valve off. The net signal minus background was accumulated until adequate image quality was obtained, typically after 15 000 total laser shots.

One experimental complication is the potential "contamination" of the images for photolysis at 230, 240, and 266 nm by signal due to dissociation by the 226 nm probe radiation alone. Careful adjustment of both the spatial and temporal overlap between the two laser pulses, coupled with the high power of the photolysis pulse, allowed images to be acquired with minimal probe contamination. The polarization of the dissociation laser was fixed throughout the experiments with its electric vector lying in a plane perpendicular to that defined by the molecular and laser beams ("vertical" polarization). Control of the probe light polarization was achieved by passing the beam through a double Fresnel rhomb. Data were collected with the polarization of the probe beam either "vertical" (perpendicular to the ion flight direction) or "horizontal" (parallel to the ion flight direction).

To eliminate this contamination a subtraction routine was used, whereby some percentage of a one-laser 226 nm horizontally polarized image was subtracted from a two-laser image also acquired with the probe polarization horizontal. Similarly, the same percentage of a one-laser vertically polarized image was subtracted from its two-laser counterpart. Typically 30% of the one-laser images were subtracted in order to minimize the differences between two-laser scans taken with the probe polarizations vertically and horizontally polarized. We note that this subtraction method is only valid if the polarization of the probe laser does not affect the detection efficiency of the fragments; i.e., it is valid provided there are no atomic $v-j$ correlations, where v is the recoil velocity and j is the angular momentum of the atomic fragment.

Results

Our experimental efforts have concentrated on the $O(^3P_2)$ formed in the minor dissociation channel, probed through a 2 + 1 REMPI scheme, at photolysis wavelengths of 226, 230, 240, and 266 nm. The raw images (except for the 266 nm dissociation image, which has been symmetrized) are shown in Figure 1. The electric vector of the dissociating light is parallel to the vertical direction in the plane of the image.

For photolysis at 226 and 230 nm the images exhibit a similar bimodal velocity distribution. However, the intensity ratios of the inner to outer portions of the images are different, with the ratio of slow (inner) to fast (outer) $O(^3P_2)$ fragments increasing for photolysis at 230 nm with respect to that at 226 nm. The velocity mapping technique increases the resolution of our data, allowing observation of structure within the inner portion of the 226 nm photolysis image; two rings are clearly apparent. The images obtained at dissociation wavelengths 240 and 266 nm display less marked bimodal velocity distributions; instead, more continuous distributions are observed.

The data displayed in Figure 1 is a two-dimensional projection of the $O(^3P_2)$ photofragment's three-dimensional velocity distribution. Because the projection is made perpendicular to the electric vector of the dissociating radiation, it is possible to reconstruct the original three-dimensional velocity distribution using the inverse Abel transform.[27] The Abel transformed slices are not shown, but they exhibit the same general features as their projected counterparts.

The recovered $O(^3P_2)$ velocity distributions from the Abel transformed slices can be separated into an angular and speed component. Angular distributions are determined by integrating over all speeds for each angle. Extraction of the speed distribution is achieved in an analogous manner by integrating over all angles for each speed. The speed distributions can be further transformed, using the law of conservation of momentum, into total translational energy distributions for the $O_3 \rightarrow O(^3P_2) + O_2(X^3\Sigma_g^-)$ dissociation. These distributions are not displayed and will be discussed in a later publication. However, for photolysis at 226 and 230 nm they are qualitatively similar to the average translational distribution for the $O_3 \rightarrow O(^3P_2) + O_2(X^3\Sigma_g^-)$ dissociation shown in Figure 2 of ref 9. The translational energy distributions obtained from our data at photolysis wavelengths of 226 and 230 nm are both strongly bimodal, peaking at energies of 0.1 and 1.7 eV with a minimum at 0.8 eV for both dissociation wavelengths.

Analysis of the $O(^3P_2)$ Angular Distributions. The $O(^3P_2)$ angular distributions have been analyzed using two different methods. The first approach assumes the data for dissociation

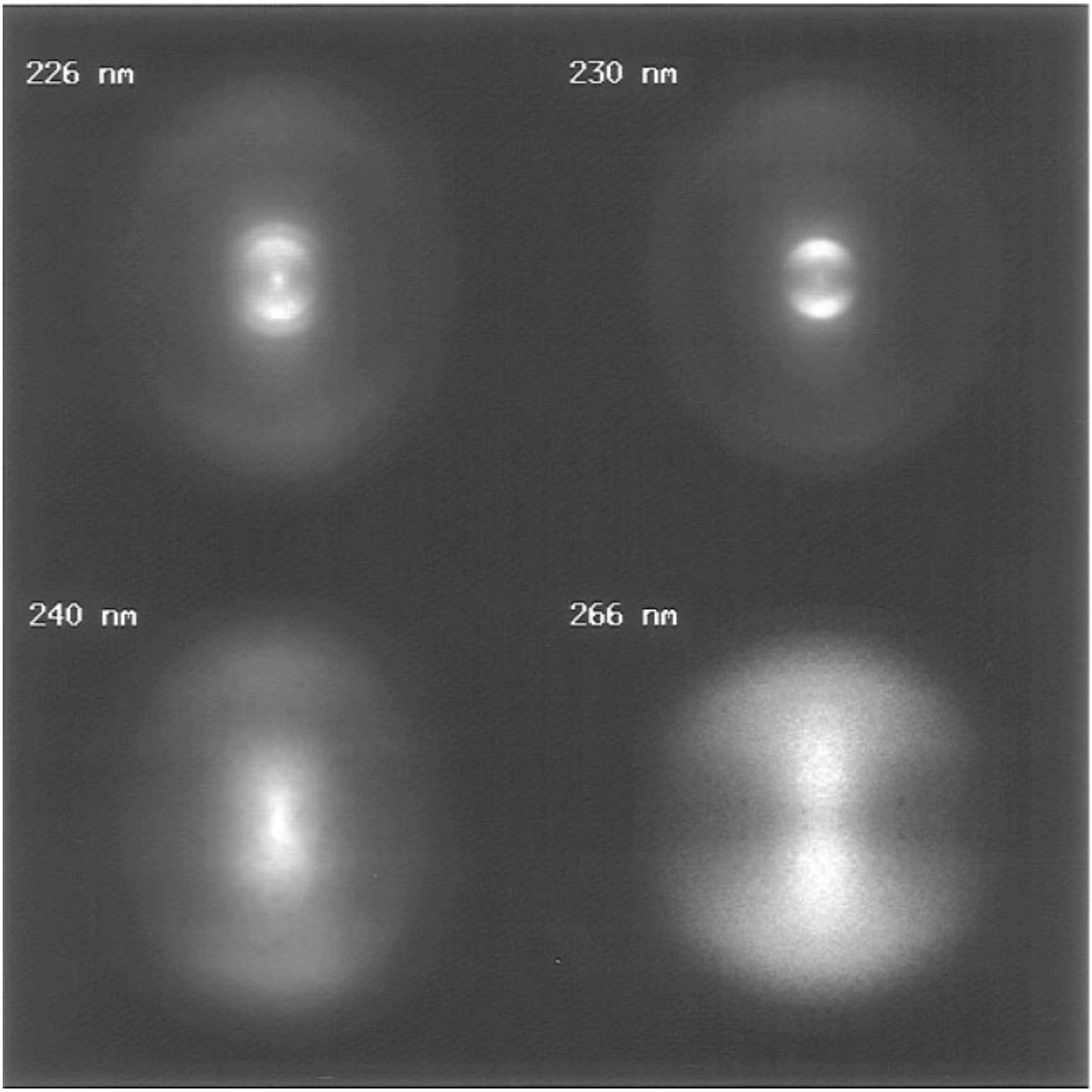

Figure 1. $O(^3P_2)$ photofragment images for photolysis wavelengths of 226, 230, 240, and 266 nm.

at 226, 230, and 240 nm to be well characterized by two β parameters, one fitted to the slow peak in the translational distribution and the other to the fast peak. Since data obtained for dissociation at 266 nm are not characterized by a clear separation between fast and slow translational speeds, the angular distribution was determined in this method by integrating over the entire speed profile of the 266 nm photolysis images. The second method of analysis makes fewer assumptions. Here the speed dependence of the $O(^3P_2)$ angular distributions is determined by examining the angular distributions obtained from a number of different speed regions of each image. This method was applied to data collected at all four dissociation wavelengths.

Two-Parameter Method. The angular distributions for the slow and fast $O(^3P_2)$ fragments have been determined separately, and typical distributions are displayed in Figure 2. The division between slow and fast fragments corresponds to the relative minimum in the $O(^3P_2)$ speed distribution, determined as 3315, 2972, and 2572 m/s for dissociation at 226, 230, and 240 nm. Figure 3 displays an angular distribution extracted from a 266 nm photolysis images. Since no bimodal velocity distributions were obvious for dissociation at this wavelength, the entire $O(^3P_2)$ velocity profiles were considered.

The solid lines in Figures 2 and 3 are fits to the data using the functional form given in eq 3 (see below); the fitted β values are listed in Table 1. The angular distributions of the slow $O(^3P_2)$ fragments are well characterized by this equation; however, the fast atom distributions we observe do not appear to be governed by a simple $\cos^2\theta$ dependence, where θ is the angle between the polarization direction of the photolysis light and the direction of recoil. The fits to the fast fragments for all three wavelengths are therefore poor.

After careful testing of our data acquisition procedure and experimental setup, we have concluded that the flat bottoms observed in the angular distributions of the fast $O(^3P_2)$ fragments are real, possibly due to alignment effects between the angular momentum of the $O(^3P_2)$ atom and the recoil velocity of the fragment. This conclusion has been borne out by preliminary analysis of $O(^3P_0)$ images from the 226 nm dissociation of ozone where no $v-j$ correlations are possible. The angular distributions obtained from these images follow a $\cos^2\theta$ dependence regardless of the fragment speed.

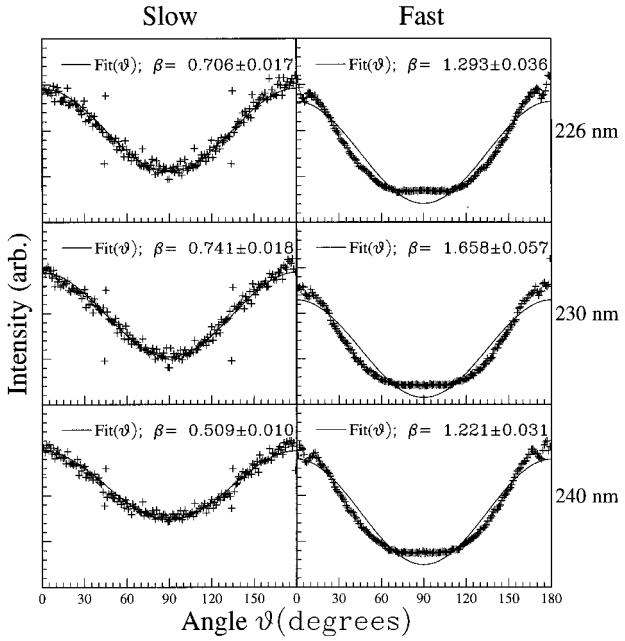

Figure 2. Angular distributions for the fast (outer) and slow (inner) $O(^3P_2)$ fragments obtained at photolysis wavelengths of 226, 230, and 240 nm. Solid line is a fit to the data of the functional form given in eq 1.

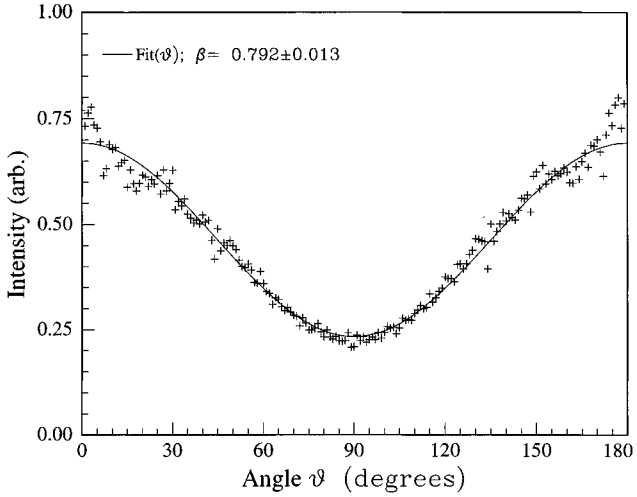

Figure 3. Angular distributions of the $O(^3P_2)$ fragments obtained for a photolysis wavelength of 266 nm. Solid line is a fit to the data of the functional form given in eq 1.

TABLE 1: Fitted β Values Obtained at Photolysis Wavelengths of 226, 230, 240, and 266 nm

	β	
dissociation wavelength (nm)	fast	slow
226	1.31 ± 0.20	0.67 ± 0.05
230	1.52 ± 0.30	0.80 ± 0.07
240	1.10 ± 0.30	0.56 ± 0.07
266	0.71 ± 0.15	0.71 ± 0.15

The exact nature of the $v-j$ correlations are the focus of further work.[26] In this investigation no attempt has been made to model or account for the suspected $v-j$ correlations at high fragment speed velocities. Instead, the breakdown of the assumptions that the angular distributions follow a $\cos^2\theta$ distribution and that the probe laser does not affect the efficiency of fragment detection, at high $O(^3P_2)$ speeds, is reflected in the magnitude of the error quoted with the anisotropy parameters.

Table 1 shows that the anisotropy parameters fitted to the angular distributions of the slow oxygen atoms are considerably smaller than those characterizing the angular behavior of the fast product pathway. A wavelength dependence is also suggested, with decreasing β values being determined as the photolysis wavelength increases.

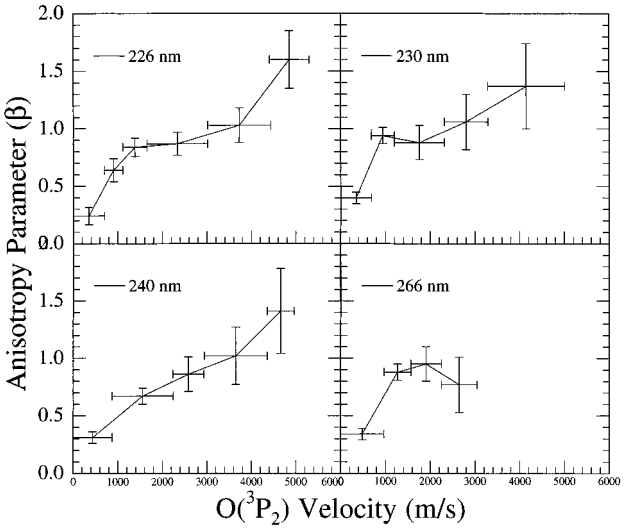

Figure 4. β versus $O(^3P_2)$ speed for photolysis at 226, 230, 240, and 266 nm.

Continuous Parameter Method. The considerable speed dependence of the anisotropy parameters characterizing the angular distributions for photolysis at 226, 230, and 240 nm prompted a more thorough investigation into the speed dependence of β for all the photolysis wavelengths considered in this work. The Abel transformed images were split into concentric speed rings. The angular distributions of the $O(^3P_2)$ fragments were then determined for each speed ring separately, and a β value was extracted by fitting the distributions to the functional form given in eq 3 (see below). The anisotropy parameters obtained are plotted in Figure 4 as a function of the average $O(^3P_2)$ fragment speed for each ring.

The broad behavior of the anisotropy parameter versus speed curves is similar for all photolysis wavelengths. Unfortunately, the 266 nm photolysis data at high $O(^3P_2)$ speeds was of insufficient quality to fit anisotropy parameters satisfactorily, so we cannot state with confidence whether the speed dependence of β changes at higher photolysis wavelengths. The overriding feature in Figure 4 is the steady increase in β as the $O(^3P_2)$ fragments travel faster. Some structure is also apparent in the curves, with a plateau between approximately 1200 and 3700 m/s.

Discussion

Angular Distributions. The angular distributions of the $O(^3P_2)$ fragments show the degree of correlation between the product recoil velocity (v) with the electric vector of the dissociating light and are typically characterized by the lab frame anisotropy parameter (β) given in the equation,[28,29]

$$I(\theta) = [1 + \beta P_2(\cos\theta)]/4\pi \qquad (3)$$

Here θ is the recoil angle relative to the electric vector of the dissociating light and P_2 is the second-order Legendre polynomial.

The anisotropy parameter is also sensitive to both the lifetime and geometry of the dissociating molecule. For an instantaneous dissociation, and assuming that the recoil velocity is directed

along the breaking bond, β can be related directly to the structure of the parent molecule by the expression

$$\beta = 2(3\cos^2\chi - 1)/2 \quad (4)$$

where χ is the angle between the transition dipole moment (μ) and the recoil velocity of the photofragment. The anisotropy parameter therefore ranges from $\beta = -1$, for a dissociation where χ is perpendicular to μ, to $\beta = 2$, where χ and μ are parallel. Since the transition moment for the $B^1B_2 \leftarrow\leftarrow \tilde{X}^1A_2$ electronic transition lies in the plane of the ozone molecule and perpendicular to the C_2 axis, the average O−O−O bond angle prior to dissociation is simply given by 180° minus 2χ.

If the photolysis process is not immediate, but instead has some finite lifetime τ, the parent molecule may have time to rotate during dissociation and so "wash out" the angular distribution. In this case a reduced effective anisotropy parameter (β_{eff}) is used to characterize the observed angular distribution. The relationship between β_{eff} and parent lifetime can be expressed as[28,30]

$$\beta_{eff} = \beta\left[\frac{1+\omega^2\tau^2}{1+4\omega^2\tau^2}\right] \quad (5)$$

where ω is the frequency of the parent rotation.

Some idea of the expected lifetime of the parent molecule leading to the triplet products can be obtained by first considering experimental studies on the singlet channel.[2,13,24,31,32] Generally, except for dissociation at 193 nm,[13] the measured (or inferred) value of β in these studies is close to the limiting anisotropy parameter of 1.18 for an instantaneous dissociation following a $B^1B_2 \leftarrow \tilde{X}^1A_1$ from the ground-state equilibrium geometry of ozone. The close agreement between the measured values of β for a number of dissociation wavelengths and the limiting anisotropy parameter indicates the dissociation must be prompt, occurring on a time scale much shorter than the rotational period of the parent molecule. This conclusion has also been drawn from theoretical studies on the B^1B_2 surface, where most of the molecules are found to dissociate within 40−60 fs.[33,34]

In the absence of a long-lived intermediate, the time constants for product formation must be the same for the two branches of the parallel reactions giving triplet products or singlet products; each appearance time is given by the reciprocal of the sum of the rates for the two parallel channels. As discussed above, the appearance time for the production of the singlet channel is thought to be prompt and constant with wavelength. Thus, barring a long-lived intermediate, the appearance time of the channel giving triplets must also be prompt and independent of photolysis energy. In this case, any variation of β with dissociation wavelength cannot be caused by a variation in the lifetime, τ, but rather must be due to a variation in the prevalent geometrical structure of the molecule immediately prior to dissociation.

Speed-Dependent Anisotropy Parameters: Two-Parameter Method. Table 1 shows that significantly different anisotropy parameters characterize the angular distributions of the fast and slow $O(^3P_2)$ fragments for photolysis at 226, 230, and 240 nm. A wavelength dependence is also suggested, with photolysis at 240 and 266 nm resulting in a more isotropic angular distribution. As discussed earlier, rotation of the excited parent molecule prior to dissociation cannot reasonably be the cause of the reduced anisotropy parameters characterizing the angular distributions of the slow oxygen atoms. Vibrational motion, however, can occur within the expected time scale for photolysis, so that the average geometry of the dissociating molecules may be different from that of the equilibrium ground-state configuration.

For dissociation at 226 and 230 nm, the determined β values for the fast and slow oxygen atoms are ∼1.3/1.5 and ∼0.7/0.8, respectively. The former value corresponds to a bond angle of ∼120°, close to the ozone ground-state equilibrium bond angle of 117°. The reduced anisotropy parameter of 0.8 implies a more strongly bent geometry with a bond angle of ∼100°.

The differing anisotropy parameters determined for the fast and slow $O(^3P_2)$ atoms strongly suggest that the two $O(^3P_2)$ velocity components sample either different potential energy surfaces or different regions of the same surface. The former situation might occur if excitation reaches more than one electronic state, whereas the latter situation might be due to multiple regions for crossing between electronic surfaces. Speed-dependent anisotropy parameters reported in the dissociation of C_2F_5I[35] and iodobenzene[36] have been rationalized by the existence of indirect photolysis channels via curve crossing. In the latter case, the photolysis lifetime also influences the relationship between the product translational energy and the angular distribution.

The bimodal velocity distribution of the $O(^3P_j)$ fragments produced via the triplet channel in the UV photodissociation of ozone has also been observed by Syage[10−12] and Stranges et al.[13] at photolysis wavelengths of 226 and 193 nm, respectively. Both authors measured anisotropy parameters for the fast and slow product pathways separately.

Our determined anisotropy parameters for 226 nm photolysis agree favorably with the reported values of Syage, where a β value of 1.2 was measured for the fast $O(^3P_2)$ products. Syage observed a less anisotropic distribution for the slow $O(^3P_2)$ atoms, with a reported β value of 0.4. The β value of 1.2 for the high-velocity component was rationalized by a prompt dissociation from the equilibrium ground state of ozone following an $B^1B_2 \leftarrow \tilde{X}^1A_1$ transition.

Syage speculated that a reduced anisotropy may be expected for the slow $O(^3P_j)$ fragments if a cyclic transition state were accessed, which would also allow the expulsion of the central oxygen atom. Such a mechanism would explain the production of vibrationally hot $O_2(^3\Sigma_g^-)$ fragments. Interestingly, theoretical calculations[37] show an intersection between the repulsive $\tilde{R}$ ($\tilde{C}$ in C_s symmetry) surface and the ground-state surface very close to the transition state for abstraction of the central oxygen. This intersection would provide an alternate route to the ground-state products via an equilateral geometry.

For photolysis at 193 nm, Stranges et al. determined β values of 0.09 and −0.33 for the fast and slow velocity components of the $O(^3P_2)$ fragments produced via the triplet channel. The considerable difference in excitation energy between Stranges study and this work makes a direct comparison between our results and theirs less meaningful. However, a brief discussion is warranted. The very small β value reported for the angular distribution of the fast velocity component was rationalized by proposing a rapid decrease in bond angle during dissociation.[34] This effect is not generally consistent with our results, and we find no manifestation of this phenomenon in the angular distributions of the fast $O(^3P_2)$ fragments at longer photolysis wavelengths. Because of the increased yield of the slow $O(^3P_2)$ atoms for dissociation at 193 nm compared to that at 226 nm, Stranges inferred that the slow product pathway originated from optical excitation not to the B^1B_2 ($\tilde{D}$ in C_s symmetry) surface but instead directly to the $\tilde{R}$ state ($\tilde{C}$ in C_s symmetry). If two electronic states are responsible for the absorption in the 226−266 nm region we have investigated, then it is possible that the variation in β with speed may be related to differing absorptions

and crossing probabilities involving these two states. However, because we do not observe negative β values for the slow oxygen atoms at photolysis wavelengths of 226 and 230 nm, and because we furthermore observe an increased yield at lower photolysis energies, it seems to us that this proposition is an unlikely explanation for our results.

At longer photolysis wavelengths, where no apparent bimodal velocity distribution is evident in our images, β decreases, yielding a value of 0.7 for dissociation at 266 nm. This value agrees well with the work of Shamsuddin et al.[38] where a β value of 0.81 was obtained for photolysis at 266 nm. Lower anisotropy parameters suggest that the prevalent transition-state geometry alters as a function of photolysis wavelength, becoming increasingly bent as the dissociation energy decreases.

Speed-Dependent Anisotropy Parameters: Continuous Parameter Method. The results of the more thorough analysis carried out on the speed dependence of β are illustrated in Figure 4. The main feature is the steady increase in anisotropy parameter as a function of increasing $O(^3P_2)$ fragment speed, as well as the similarity of the curves for dissociation at 226, 230, 240, and 266 nm. The β versus fragment speed plots also appear to have a plateau occurring at a value 0.8 with an onset at 1200 m/s; this structure is more prevalent in the 226 and 230 nm photolysis data. Although a speed-dependent anisotropy parameter was expected and had been partially uncovered for the bimodal 226 and 230 nm photolysis images, the similarity and strength of the speed dependence for the β values extracted from the 240 and 266 nm data were not anticipated.

Figure 4 provides us with a more complete picture of the dissociation process with our results indicating the following points: (1) The $O(^3P_2)$ speed dependence of β is insensitive to the dissociation wavelength, yet the probability of an $O(^3P_2)$ fragment having a particular speed is a function of photolysis energy. (2) The excited ozone molecules do not photolyze immediately but do so instead on a time scale that allows the excited molecules to bend. The β values obtained correspond to bond angles varying from ~80° to ~130°. (3) The structure of the dissociating state is directly correlated to the partitioning of available energy between the translational and internal energies of the resulting $O(^3P_2)$ and $O_2(^3\Sigma_g^-)$ photofragments. The increasingly bent parent molecules favor slow products and vibrationally hot $O_2(^3\Sigma_g^-)$ fragments, while those with more obtuse bond angles result in fast products in coincidence with vibrationally cooler $O_2(^3\Sigma_g^-)$ fragments.

The steady increase in β with fragment speed could possibly be explained if many different regions of the same potential surface were sampled by the dissociating molecules. The obvious manner for this sampling to occur would be along the crossing seam between the initially excited B^1B_2 surface and the repulsive $\tilde{R}$ state correlating to the triplet products. A possible explanation that qualitatively accounts for the main features of our data trends comes from predicting the expected dynamics for molecules crossing at different points between these two surfaces.

First consider the expected crossing between the B^1B_2 surface and repulsive $\tilde{R}$ state along the symmetric stretch coordinate. We can plausibly expect the surfaces to interact in more than one region even though the asymptotes correlating to the dissociation products along the symmetric and asymmetric stretch coordinates of the B^1B_2 state lie higher in energy than the corresponding asymptotic limits of the $\tilde{R}$ state. This interaction is possible, providing the upper state surface is shallower along the symmetric stretch coordinate than the $\tilde{R}$ state. Figure 5 is a two-dimensional schematic of the repulsive surface and illustrates how the intersection between the two states might appear.

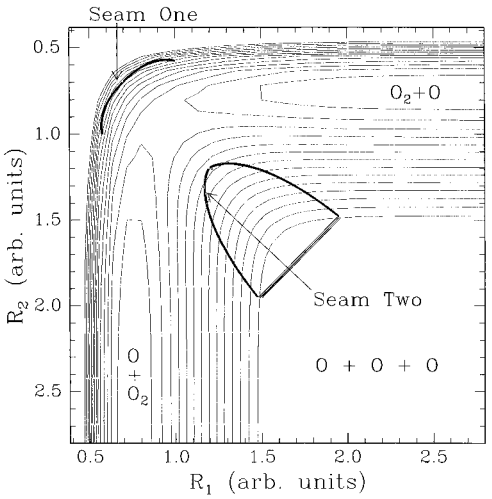

Figure 5. Schematic of the repulsive surface correlating to the triplet products illustrating the two crossing regions of the initially excited B^1B_2 surface.

We can now imagine two illustrative cases for nonadiabatic transitions between the B^1B_2 and $\tilde{R}$ states: one where the crossing takes place at a point along seam "one" and the second where the crossing point lies along seam "two". In the first case, the transition is made when the ozone bond lengths are little extended, and the molecules move onto the repulsive surface at a point relatively close to the minimum-energy pathway. Such a trajectory will impart energy into both the vibration of the oxygen diatomic and the translational of the fragments. If, however, the transition between the two surfaces is made when the ozone bond lengths are considerably extended, we can imagine a scenario where the molecules would move onto the repulsive surface at a point on the second crossing seam directly above (in energy) the valley leading to dissociation. As the molecules move down this hill and into the valley, they are traveling more nearly perpendicular to the dissociation coordinate and so do not follow the minimum-energy path. A trajectory such as this will "oscillate" up and down the valley walls (the bobsled effect) on its way to dissociation and impart energy to the vibrational coordinate of the $O_2(^3\Sigma_g^-)$ fragment at the expense of translation.

It is unclear exactly how the two potential surfaces, and hence the interaction regions between them, behave as the parent molecules bend. Our experimental results indicate that the more bent the ozone molecules are as they dissociate the more effectively is the available energy channeled into the $O_2(^3\Sigma_g^-)$ fragment vibration. It is possible that as the parent molecules bend, the crossing seams move to a region on the repulsive state that more strongly favors the production of vibrationally excited $O_2(^3\Sigma_g^-)$ fragments.

The dynamics of the two illustrative examples show how our results could be rationalized by considering the crossing points between the two surfaces. The scenarios presented would explain both the insensitivity of the $O(^3P_2)$ fragments speed-dependent angular distributions with regard to photolysis energy and also the correlation we observe between parent geometry and the degree of vibrational excitation in the $O_2(^3\Sigma_g^-)$ molecules. Our experimental results indicate that the probability of an $O(^3P_2)$ fragment being produced with a certain speed is dependent on excitation energy. This dependence could be incorporated into our conceptual model if the likelihood of crossing at a particular point on the seams is influenced by the excitation wavelength.

Although the above discussion seems reasonable, its difficult either to take it much further or even to ascertain the likelihood of the scenarios presented without more detailed three-dimensional calculations on the nonadiabatic crossing region between the B^1B_2 and $\tilde{R}$ surfaces.[4,32,36−39] It should be stressed that the scenarios are not presented as an exact mechanism but rather as a speculative model that qualitatively explains the trends in our data.

Conclusions

Two-dimensional product imaging has been used to determine the speed dependence of the $O(^3P_2)$ fragment formed in the UV dissociation channel of ozone. For dissociation at 226 and 230 nm, the probed oxygen atoms exhibit bimodal velocity distributions; this bimodality becomes less evident for photolysis at 240 and 266 nm. The anisotropy parameters determined for all four dissociation wavelengths show a similar and marked dependence on $O(^3P_2)$ fragment speed: β increases with oxygen atom speed. This dependence translates to a strong correlation between the average ozone bond angle prior to dissociation and the partitioning of available energy between the translational and internal energies of the photofragments. A tentative model for the dissociation dynamics leading to the triplet channel is introduced which intuitively predicts the broad features of our data trends.

Acknowledgment. This work was supported by the National Science Foundation under Grant ATM-9528086 and, in part, by the Research Institute of Innovative Technology for the Earth administered by the New Energy and Industrial Technology Development Organization of Japan. R.J.W. thanks The Royal Society of Chemistry and NATO for the award of a NATO Fellowship. We also thank Dr. Bor-Yu Chang for his help and ideas.

References and Notes

(1) Hay, P. J.; Pack, R. T.; Walker, R. B.; Heller, E. J. *J. Phys. Chem.* **1982**, *86*, 862.
(2) Fairchild, C. E.; Stone, E. J.; Lawrence, G. M. *J. Chem. Phys.* **1978**, *69*, 3632.
(3) Sparks, R. K.; Carlson, L. R.; Shobatake, K.; Kowalczyk, M. L.; Lee, Y. T. *J. Chem. Phys.* **1980**, *72*, 1401.
(4) Amimoto, S. T.; Force, A. P.; Wiesenfeld, J. R.; Young, R. H. *J. Chem. Phys.* **1980**, *73*, 1244.
(5) Brock, J. C.; Watson, R. T. *Chem. Phys. Lett.* **1980,** *71*, 371.
(6) Greenblatt, G. D.; Wiesenfeld, J. R. *J. Chem. Phys.* **1983**, *78*, 4924.
(7) Valentini, J. J.; Gerrity, D. P.; Phillips, D. L.; Nieh, J.-C.; Tabor, K. D. *J. Chem. Phys.* **1987**, *86*, 6745.
(8) Turnipseed, A. A.; Vaghjiani, G. L.; Gierczak, T.; Thompson, J. E.; Ravishankara, A. R. *J. Chem. Phys.* **1991**, *95*, 3244.
(9) Miller, R. L.; Suits, A. G.; Houston, P. L.; Toumi, R.; Mack, J. A.; Wodtke, A. M. *Science* **1994**, *265*, 1831.
(10) Syage, J. A. *J. Phys. Chem.* **1995**, *99*, 16530.
(11) Syage, J. A. *J. Phys. Chem.* **1996**, *100*, 13885.
(12) Syage, J. A. *J. Chem. Phys.* **1996**, *105*, 1007.
(13) Stranges, D.; Yang, X.; Chesko, J. D.; Suits, A. G. *J. Chem. Phys.* **1995**, *102*, 6067.
(14) Toumi, R.; Houston, P. L.; Wodtke, A. M. *J. Chem. Phys.* **1996**, *104*, 775.
(15) Houston, P. L.; Suits, A. G.; Toumi, R. *J. Geophys. Res.* **1996**, *101*, 18829.
(16) Price, J. M.; Mack, J. A.; Rogaski, C. A.; Wodtke, A. M. *Chem. Phys.* **1993**, *175*, 83.
(17) Elluskiewicz, J.; Allen, M. *J. Geophys. Res.* **1993**, *98*, 1069.
(18) Toumi, R.; Kerridge, B. J.; Pyle, J. A. *Nature* **1991**, *351*, 217.
(19) Crutzen, P. J.; Grooss, J.-U.; Brühl, C.; Müller, R.; Russell, J. M. *Science* **1995**, *268*, 705.
(20) Jucks, K. W.; Johnson, D. G.; Chance, K. V.; Traub, W. A.; Salawitch, R. J.; Stachnik, R. A. *J. Geophys. Res.* **1996**, *101*, 28785.
(21) Dessler, A. E.; Kawa, S. R.; Considine, D. B.; Waters, J. W.; Froidevaux, L.; Kumer, J. B. *Geophys. Res. Lett.* **1996**, *23*, 339.
(22) Siskind, D. E.; Connor, B. J.; Eckman, R. S.; Remsberg, E. E.; Tsou, J. J.; Parrish, A. *J. Geophys. Res.* **1995**, *100*, 11191.
(23) Chandler, D. W.; Houston, P. L. *J. Chem. Phys.* **1987**, *87*, 1445.
(24) Suits, A. G.; Miller, R. L.; Bontuyan, L. S.; Houston, P. L. *J. Chem. Soc., Faraday Trans.* **1993**, *89*, 1443.
(25) Eppink, A. T. J. B.; Parker, D. H. Velocity map imaging of ions and electrons using electrostatic lenses; Application in photoelectron and photofragment ion imaging of molecular oxygen. To be published.
(26) Wilson, R. J.; Mueller, J. A.; Houston, P. L. Manuscript in preparation.
(27) Castleman, K. R. *Digital Image Processing*; Prentice-Hall: Englewood Cliffs, NJ, 1979.
(28) Busch, G. E.; Wilson, K. R. *J. Chem. Phys.* **1972**, *56*, 3638.
(29) Zare, R. N.; Herschbach, D. R. *Proc. IEEE* **1963**, *51*, 173.
(30) Jonah, C. *J. Chem. Phys.* **1971**, *55*, 1915.
(31) Thelen, M.-A.; Gejo, T.; Harrison, J. A.; Huber, J. R. *J. Chem. Phys.* **1995**, *103*, 7946.
(32) Levene, H. B.; Valentini, J. J. *J. Chem. Phys.* **1987**, *87*, 2594.
(33) Chasman, D.; Tannor, D. J.; Imre, D. G. *J. Chem. Phys.* **1988**, *89*, 6667.
(34) Leforestier, C.; Le Quéré, F.; Yamashita, K.; Morokuma, K. *J. Chem. Phys.* **1994**, *101*, 3806.
(35) Hwang, H. J.; El-Sayed, M. A. *Chem. Phys. Lett.* **1990**, *170*, 161.
(36) Freitas, J. E.; Hwang, H. J.; El-Sayed, M. A. *J. Phys. Chem.* **1993**, *97*, 12481.
(37) Xantheas, S. S.; Atchity, G. J.; Elbert, S. T.; Ruedenberg, K. *J. Chem. Phys.* **1991**, *94*, 8054.
(38) Shamsuddin, S. M.; Inagaki, Y.; Matsumi, Y.; Kawasaki, M.; *Can. J. Chem.* **1994**, *72*, 637.
(39) Balakrishnan, N.; Billing, G. D. *J. Chem. Phys.* **1994**, *101*, 2968.
(40) Banichevich, A.; Peyerimhoff, S. D. *Chem. Phys.* **1993**, *174*, 93.
(41) Banichevich, A.; Peyerimhoff, S. D.; Grein, F. *Chem. Phys.* **1993**, *178*, 155.
(42) Sheppard, M. G.; Walker, R. B. *J. Chem. Phys.* **1983**, *78*, 7191.
(43) Yamashita, K.; Morokuma, K.; Le Quéré, F.; Leforestier, C. *Chem. Phys. Lett.* **1992**, *191*, 515.